


Topologically protected edge and confined states in finite armchair graphene nanoribbons and their junctions

M. Pilar López-Sancho  and M. Carmen Muñoz

Instituto de Ciencia de Materiales de Madrid, CSIC, Calle Sor Juana Ines de la Cruz 3, Cantoblanco, 28049 Madrid, Spain

 (Received 20 August 2021; revised 10 November 2021; accepted 15 November 2021; published 3 December 2021)

Topologically protected edge and junction states, previously predicted, have recently been observed in armchair graphene nanoribbon (AGNR) heterojunctions. Here, via tight-binding-based calculations, we explain the relation between the nature and number of the zero-mode edge states of finite-length AGNRs and their structure, topological invariants, and winding number. This allows us to rationalize the design of AGNR heterojunctions and superlattices with tailored phases. We show how the choice of widths, interface coupling geometry, and boundaries determines the emergence of topological states following patterns that depend on the structure and family of the constituent AGNRs. Furthermore, we prove that quantum-well-like states confined in one of the constituent ribbons develop in all the AGNR junctions irrespective of their trivial or topological character. The bipartite nature of the honeycomb lattice is determinant for the topological properties of the junctions: their electronic states can be topologically trivial or nontrivial depending on subtle differences at the boundaries of the ribbons.

DOI: [10.1103/PhysRevB.104.245402](https://doi.org/10.1103/PhysRevB.104.245402)

I. INTRODUCTION

New advances in the fabrication of graphene ribbons by bottom-up synthesis using molecular precursor led to the realization and characterization of ribbons of nanometric width and well-defined edge shapes with atomically precise control of their structural parameters [1–4]. The properties of the bottom-up synthesized ribbons are accurately tuned by designing their width and termination shape. As recent work has recognized, graphene ribbons are quasi-one-dimensional (1D) topological materials, topological order being fundamental to understanding their properties. Although graphene nanoribbons, as carbon nanotubes, have been widely investigated their topological character has boosted new efforts and triggered renewed theoretical and experimental work; in particular, armchair graphene nanoribbons (AGNRs) have drawn great attention. An important achievement in this context has been the experimental realization of heterojunctions of different graphene nanoribbons (GNRs) [5,6]. Due to their topology AGNRs can present exotic quantum phases with robust edge states protected against defects and impurities, thus offering promising potential for the fabrication of nanoelectronic and spintronic devices [7,8]. In addition, the possibility of engineering topological states is essential for the emerging field of quantum information [9–13].

In a seminal paper Cao *et al.* [14] derived the relation between the band topology and the atomic structure of AGNRs, predicting the existence of symmetry-protected topological states in junctions of AGNRs with distinct topological character. It was shown that the topological phase of laterally confined semiconducting AGNRs is determined by their width and terminating crystallographic unit cell and is characterized by a Z_2 invariant [15], the classification in-

dex that differentiates topological insulators ($Z_2 = 1$) from trivial insulators ($Z_2 = 0$) in gapped 1D systems [16]. Z_2 topological classification requires both time-reversal and spatial symmetry. Topological bound states were actually observed in 1D periodically modulated semiconductor AGNRs, in which the Z_2 invariant was tuned through the width and unit cell edge termination of AGNRs [17,18]. Topological end states have also been detected in finite ultranarrow AGNRs [19] and a metal-insulator transition was predicted as a function of the ribbon length in the five-atom-width AGNR [20].

The explicit categorization of the symmetry-protected Z_2 topological classification was extended beyond AGNRs to any type of termination with spatial symmetry [9] and topological states were successfully engineered at the junction between GNR segments of different widths and diverse edge shapes, such as cove or chevron edges and with varying topological character [14,17,18,21].

Although the component segments of topological AGNR junctions have the same crystalline lattice, the inversion or mirror symmetry of the constituent ribbons is broken at the interface and the point group of the junction is reduced. So, based on the chiral symmetry a Z classification, which does not require time-reversal and spatial symmetry, was later proposed for GNRs [22,23]. This classification can be applied to any chiral-symmetric systems, and since chiral symmetry is an approximate symmetry of graphene, a simple analytic expression was derived for the Z invariant of graphene structures. Based on the Z invariant, topological bound states can be engineered in a broad class of structures including junctions with an intermediate section, multiway junctions composed of three or more AGNRs, and even two-dimensional (2D) networks [23]. Therefore, the Z classification contributes to the understanding of topological features in 1D systems and

provides design rules for novel graphene arrangements [24]. The sublattice symmetry is of crucial importance for the topology and has been invoked to design zero-energy boundary states in all systems, both crystalline and amorphous, that have chiral symmetry [25].

In this work, we investigate the emergence of topological and confined states in finite AGNRs and junctions of distinct AGNRs. In particular, we have examined the evolution of the electronic structure and topological properties depending on the width, length, and termination of AGNRs, addressing the emergence of topological edge states at the zigzag ends of finite ribbons and at the boundaries of junctions. Additionally, the development of coupled topological interface states, when distinct AGNRs are periodically arranged in a superlattice, is analyzed.

We provide the topological class selection of AGNRs for both the Z and Z_2 topological classifications, identifying the topologically nontrivial AGNRs. We prove that the Z invariant determines the number of zero-dimensional topological in-gap states at the ribbon termination and that a difference between invariants, either Z or Z_2 , other than zero reflects the presence of protected interface states within the gap of the AGNR junctions. We have also shown the emergence of topological states in nominal metallic ribbons and we demonstrate that trivial states in AGNR junctions are laterally confined to only one of their constituent segments. Furthermore, adjusting the length of the ribbons that form the junction, the energy and coupling of both topological and nontopological states can be controlled.

II. MODEL AND METHOD

The calculations are based on the tight-binding model, which captures the essential physics of graphene. We perform two types of calculations, either with the four-orbital $2s, 2p_x, 2p_y, 2p_z$ basis set or with only the p_z orbital. The empirical tight-binding Hamiltonian takes the form

$$H_0 = \sum_{i,\alpha,\sigma} \epsilon_{i,\sigma}^\alpha + \sum_{(i,j),\alpha,\beta,\sigma} t_{ij}^{\alpha,\beta} c_{i,\sigma}^{\alpha\dagger} c_{j,\sigma}^\beta + \text{H.c.}, \quad (1)$$

where ϵ^α represents the atomic energy of the orbital α , i, j stand for atomic sites of the honeycomb lattice, and $c_{i,\sigma}^{\alpha\dagger}$ and $c_{i,\sigma}^\alpha$ are the creation and annihilation operators of one electron at site i , orbital α , and spin σ , respectively.

The Hamiltonian is built following the Slater-Koster formalism up to the nearest-neighbor hopping. For the four-orbital basis set we use the Tomanek-Louie parametrization for graphite [26] while in the p_z -orbital model the on-site energy ϵ is set to zero and the nearest-neighbor hopping integral t_{ij} to 2.66 eV which coincides with the $pp\pi$ parameter of Ref. [26]. The two bases give the same results for the energy as well as for the parity and symmetry of the wave functions, for states around the zero energy [27,28], that is, for states lying close to the Fermi energy (see the Appendix).

The choice of the tight-binding (TB) approach instead of first-principles calculations allows us to study GNRs of a long length with a large number of atoms. It is also well known that the tight-binding model satisfactorily describes the low-energy physics of graphene nanostructures. Although *ab initio* methods, such as density functional theory (DFT)

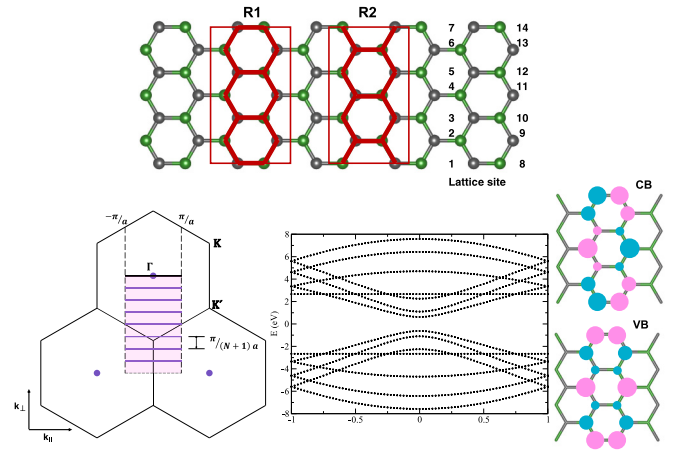


FIG. 1. Top: Schematic lattice structure of the 7-AGNRs. The geometry of the R1 and R2 unit cells is shown. Bottom: Graphene and AGNR Brillouin zones; the allowed transverse wavenumbers for the 7-AGNR are represented (left). Band structure of the 7-AGNR (center). Spatial distribution of the valence- and conduction-band wave functions at the Γ point on the lattice site positions across the ribbon (right). Blue and pink indicate positive and negative amplitudes, respectively.

calculations, include additional information to that considered in the tight-binding model, a comparison of the results shows a correspondence in symmetry and in dispersion of the significant energy bands [29]. In fact experimental results [10,18,30] note the good agreement observed for the GNR heterojunction frontier bands with the band structures obtained by DFT and TB calculations, close to the Fermi energy.

For the sake of clarity we present here results obtained with the one-orbital p_z tight-binding Hamiltonian and thus they show electron-hole symmetry. As stated before, calculations performed with the four-orbital basis give similar results with negligible variations of the band energies, especially in the zero-energy region since these low-energy states are of pure p_z character. When considering heterojunctions the same hopping parameters are used for all the constituent ribbons and also in the calculation of the junction properties, in contrast with other works [17,19].

The atomic structure of the junction at the interface is simply the one that results from coupling the two adjacent ribbons without including intermediate extra segments. We do not consider edge relaxation or passivation.

III. ARMCHAIR GRAPHENE NANORIBBONS

A. Infinite ribbons

The electronic properties of graphene nanoribbons depend on their geometry: width, length, and edge shape [31–33]. Armchair GNRs, whose edges are formed by dimers of atoms of the two sublattices, can be classified into three families, $N = 3p$, $N = 3p + 1$, and $N = 3p + 2$, where N represents the number of transverse carbon atom rows determining the width of the ribbon, and p is an integer (see Fig. 1). In the tight-binding model, the first two families exhibit semiconducting behavior with band gaps inversely proportional to their width and approaching zero in the limit of very large

TABLE I. Topological invariants Z_2 and Z calculated following the expressions given in Refs. [14,22] for AGNRs of the three families with the R1 and R2 unit cells. In the first row, W is the number in parentheses. In the second row, p is the number in parentheses.

(W)	$6(0) + 3$	$6(1) - 1$	$6(1) + 1$	$6(1) + 3$	$6(2) - 1$	$6(2) + 1$	$6(2) + 3$	$6(3) - 1$	$6(3) + 1$
(p)	$3(1)$	$3(1) + 2$	$3(2) + 1$	$3(3)$	$3(3) + 2$	$3(4) + 1$	$3(5)$	$3(5) + 2$	$3(6) + 1$
N	3	5	7	9	11	13	15	17	19
Z_2 (R1)	0	1	1	1	0	0	0	1	1
Z_2 (R2)	1	0	0	0	1	1	1	0	0
Z (R1)	0	1	1	1	2	2	2	3	3
Z (R2)	1	2	2	2	3	3	3	4	4

N [33,34]. The $N = 3p + 1$ family presents the largest gap while ribbons of the third family show a metallic behavior in agreement with some experiments reporting nearly metallic character of 5- and 17-AGNRs [2,7,35,36]. DFT and more realistic calculations predict edge relaxation that opens a small gap in the band structure of $N = 3p + 2$ AGNRs. The inclusion of many-electron interactions also produces a gap in metallic armchair ribbons [37]. These trends can be understood by considering the discrete k quantization in the direction perpendicular to the AGNR axis. Considering only nearest-neighbor hopping between carbon atoms, the wave function of the AGNR must vanish beyond the carbon atoms at the armchair edge [38,39]. The transverse wavenumber k_n is thus determined through the edge boundary condition and takes the values $k_n = 2\pi n / (N + 1)a_{gr}$, $n = 1, 2, 3, \dots, N_i$, where a_{gr} is the lattice constant of graphene.

Hence, the energy band structure of AGNRs is obtained by slicing the band structure of graphene at the allowed k_n ; the K and K' valleys are coupled at the armchair edges. In the case of the $N = 3p + 2$ family the allowed k_n coincide with the Dirac point of the graphene band structure. Figure 1 shows the atomic and electronic band structure of the $N = 7$ AGNR, representative of the $3p + 1$ family; the discrete transverse wave numbers determined by the edge boundary condition are shown in the first Brillouin zone (BZ) of graphene. The top of the valence band and the bottom of the conduction band are located at $k = 0$ and, as a direct consequence of the band gap opening, electrons in AGNRs of the $N = 3p + 1$ and $N = 3p$ families cannot be considered as massless Dirac fermions but they exhibit a finite effective mass. Their wave functions have a phase difference between A and B sublattice sites owing to the chiral nature of graphene [40]. Figure 1 also shows the distribution of the 7-AGNR highest valence- and lowest conduction-band wave functions at the Γ point. While the top of the valence band is even under the mirror and inversion symmetries of the unit cell (u.c.), the lowest conduction subband is odd.

As stated in the introduction GNRs are quasi-1D topological materials. Their topology is dictated by the spatial symmetry, width, and termination type. The AGNRs' symmetry-protected topological phases can be classified by the Z_2 invariant [14]. The Z_2 index derives from the Zak phase [15], which in 1D systems depend on the shape of the unit cell, and has two contributions: the intracell and the intercell parts, the latter being quantized at zero or π if the system has spatial symmetries such as inversion and/or mirror. Since spatial symmetry may no longer be preserved at the AGNR frontiers, an alternative Z classification applicable to general

1D systems with chiral symmetry was established, leading to a Z invariant [22,23], which takes integer values in contrast to Z_2 . Chiral symmetry is exact in bipartite lattices, in which the system can be divided into two sets of atoms, sublattices A and B, such that interactions only exist between atoms of different sublattices. Thus, chiral symmetry is an approximate symmetry of graphene and AGNRs have chiral symmetry if second-nearest-neighbor interactions are neglected. Hence, the different topological phases of an AGNR can also be labeled by this integer Z topological invariant related to the winding number and, according to the modern theory of polarization, to the bulk polarization of a periodic system [41,42]. Because of the bulk-edge correspondence, topological bound states emerge at the interface of AGNRs belonging to different Z_2 or Z classes [43,44].

Therefore, the value of the Z_2 and Z invariants depends on the width of the AGNR and the shape of its termination, which dictates a unique bulk unit cell. Simple analytical expressions were derived for various terminations [14,22]. They yield the topological invariants as a function of N , the number of transverse carbon atom rows determining the width of the ribbon. Table I gives the Z_2 and Z invariants of several AGNRs for two different choices of the 1D bulk unit cell (u.c.), R1 and R2 (see Fig. 1). We restrict ourselves to AGNRs formed by an odd number of rows across their width, $N = \text{odd}$, although our results can be generalized to even N ribbons. For $N = \text{odd}$ both R1 and R2 terminations have inversion and mirror symmetry, and the three families of AGNRs alternate when increasing the width. Both invariants show an $N = 6$ variation and the shape of the unit cell determines the topological class of the ribbon. The Z_2 invariant takes opposite values for the R1 and R2 u.c., while the integer Z invariant increases by one unit when the ribbon width is increased by six rows. Moreover, for a specific AGNR Z is always one more unit for the R2 geometry than for the R1. Alternatively to the previous $N = 3p$, $N = 3p + 1$, and $N = 3p + 2$ description of the AGNR families, the ribbon width N can be also described by the corresponding winding number W : $N = 6W - 2, 6W - 1, 6W, 6W + 1, 6W + 2$, and $6W + 3$ (W being an integer). For $N = \text{odd}$ the semiconductor ribbons correspond to $N = 6W + 1$ and $6W + 3$, while $N = 6W - 1$ are metallic [23]. The description in terms of W is directly related to the Z invariant as can be seen in Table I.

B. Finite-length ribbons: Zero-mode edge states

We have calculated the electronic structure of a large number of AGNRs with both types of unit cell, R1 and R2. When periodic boundary conditions (PBCs) are imposed to

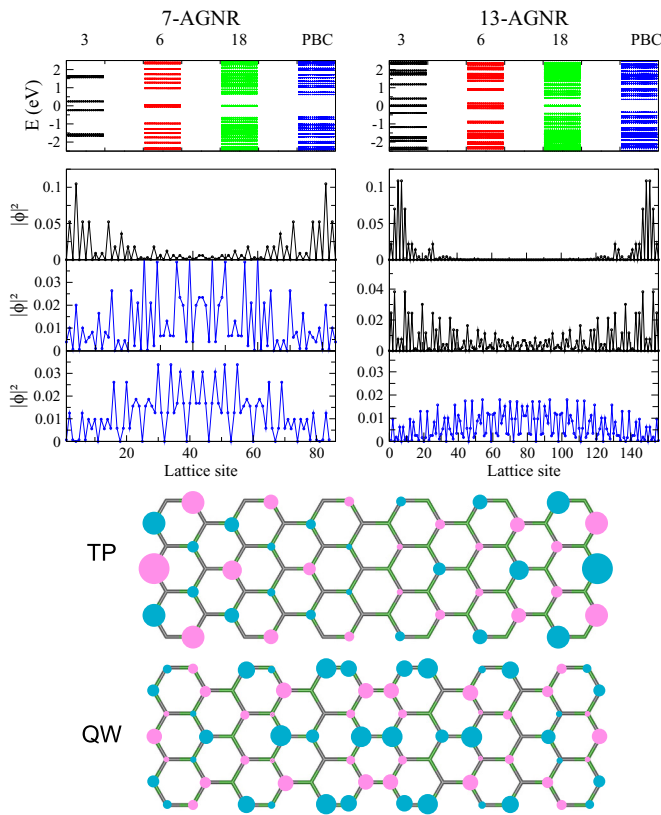


FIG. 2. Top: TB energy spectrum for a finite 7-AGNR (left) and 13-AGNR (right) of R1 geometry, with lengths of 3, 6, and 18 u.c. and with periodic boundary conditions (PBCs). Middle: Wave function amplitude density $|\phi|^2$ per C lattice site, at the Γ point, for the 7-AGNR (left) and 13-AGNR (right) corresponding to the first (top), second (middle), and third (bottom) occupied states for a ribbon of 6 u.c. length. Bottom: Wave function distribution for the two first occupied states corresponding to the 7-AGNR. Blue and pink indicate positive and negative amplitudes, respectively.

an N -AGNR, no differences are found, either between the band structures or in the amplitude distribution of the wave functions for the R1 and R2 unit cell geometries. The wave functions corresponding to the highest occupied valence and lowest unoccupied conduction states extend along the ribbon, independently of the different topological invariants of both geometries. These states are of pure π character. Therefore, the bulk band structure is unchanged when comparing infinite ribbons displaced by several atoms [45].

However, when considering finite-length ribbons, marked differences appear between their electronic properties for the two types of border. Figure 2 shows the energy spectrum obtained from the tight-binding Hamiltonian for the symmetrical finite-length 7- and 13-AGNRs with the termination R1, for three different lengths. They are the narrowest ribbons belonging to the $3p + 1$ ($6W + 1$) family. Because of their semiconductor character, topological states (TSs) arise within the gap for both AGNRs, and their energies approach zero as the length of the ribbon increases. The zero-dimensional (0D) states are only spin degenerated and always appear in conjugated pairs, one in the valence band and one in the conduction band, due to the presence of two equal terminations in the

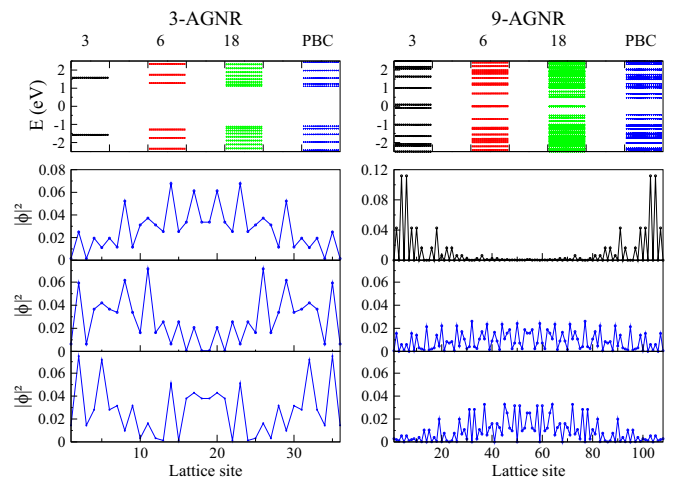


FIG. 3. Same as Fig. 2 for the 3-AGNR (left) and 9-AGNR (right).

symmetric ribbons. In the 7-AGNR, there is just one pair of TSs within the energy gap of the infinite-length ribbon, while there are two pairs in the 13-AGNR. Both AGNRs belong to the same family, and their gaps in the p_z model are $E_g = 1.24$ and 0.7 eV for the 7-AGNR and 13-AGNR, respectively. The spatial distributions of TSs are also depicted in Fig. 2, showing that they are mainly localized on the two zigzag edges at the frontiers of the ribbons with vacuum. They are confined to the atoms of a sublattice, different in the left and right edges. The parities of the wave functions under mirror and inversion symmetries are even and odd for the valence and conduction TSs, respectively. Further, their spatial extension is almost independent of the length of the AGNR, while their energy is modulated by the number of unit cells in the ribbon. Thus, the atom-projected local density of states (LDOS) is almost the same for the three finite-length ribbons shown in the figure. The amplitude decreases with the distance to the edges, being minimal at the central atoms. There is one electron accommodated in each state. For ribbons of about 100 unit cells in length, TSs are located at zero energy and become one-edge states, the amplitude of their wave functions being confined to only one of the borders.

The rest of the states bracketing the topological edge states extend to the entire length of the AGNR following the quantization pattern of confined states and accumulate in the energy ranges of the bulk bands as the length of the AGNR increases.

This behavior is common to all the ribbons of the two semiconductor families except the 3-AGNR which never presents topological states in the semiconductor gap, regardless of the length of the ribbon. The eigenvalues of the 3-AGNR for three different lengths are represented in Fig. 3 together with those corresponding to the 9-AGNR with a pair of conjugated TSs in the semiconductor gap. The confined state quantification pattern is particularly transparent for the narrowest 3-AGNR formed by a linear chain of simple hexagons.

However, for metallic ribbons the behavior of the states around zero energy differs. The energy spectrum of the representative 5-AGNR and 11-AGNR are displayed in Fig. 4. The low-energy states of the 5-AGNR are equally separated in energy, reflecting the linear dispersion of metallic ribbons, and those closest to zero only reach the energy zero for

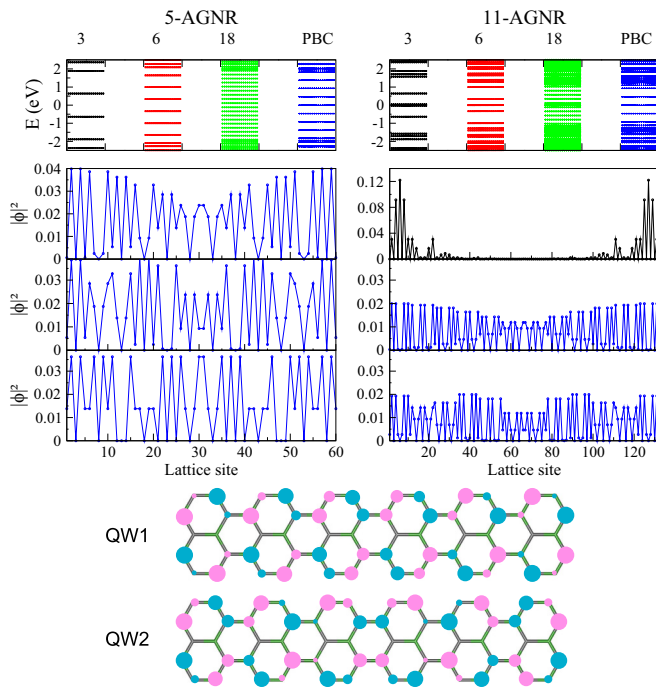


FIG. 4. Same as Fig. 2 for the 5-AGNR (left) and 11-AGNR (right). The wave function distributions correspond to the two first occupied states of the 5-AGNR.

very long ribbons. For example, the highest occupied state of the 100 u.c. 5-AGNR appears at -0.0625 eV. Moreover, the amplitude of their wave function, although slightly larger at the atoms of the two edges, is significant throughout the entire ribbon. Therefore, the 5-AGNR does not hold TSSs. Surprisingly, despite its metallic character, localized topological modes emerge in the 11-AGNR. Its energy is almost zero even for ribbons as short as 3 u.c. in length and are perfectly localized at the edges. In addition, extended modes with the same energy and spatial distribution of the wave function as those of the 5-AGNR are also present.

When the termination of the finite-length AGNRs corresponds to the R2 geometry, a pair of new zero-mode states emerges independently of the family or length of the ribbon. These zero modes are truly localized edge states; their wave function amplitude presents maxima on the zigzag atoms of one edge and zero on the rest. Figure 5 shows the energy spectrum and atom-projected LDOS of three representative AGNRs of very short length, 3 u.c. In all the ribbons, in addition to the zero modes, TSSs equal to those of the corresponding ribbon with the R1 termination appear.

According to Table I, the Z_2 invariant of the semiconductor 7- and 9-AGNR with the R1 unit cell is 1 (topologically nontrivial), whereas that of the 13-AGNR is zero (topologically trivial). Otherwise, the Z invariant, directly related to the winding number, takes the values 1 for the 7- and 9-AGNR and 2 for the 13-AGNR with the R1 unit cell. Moreover, with the R2 unit cell, Z_2 has the opposite value and Z increases by one unit. Therefore, the number of edge states in the band gap of all the semiconductor AGNRs, without counting the spin degree of freedom, coincides with the value of Z independently of the value of Z_2 , zero or 1. Consequently, the number

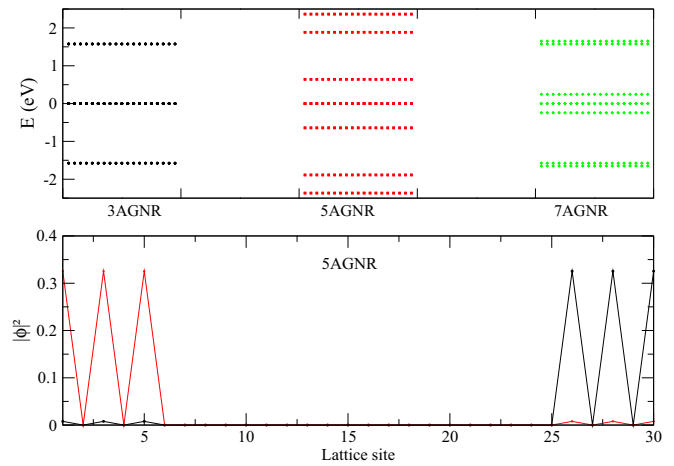


FIG. 5. Top: Energy spectrum of finite 3-, 5-, and 7-AGNR of R2 geometry with 3 u.c. in length. Bottom: Amplitude density $|\phi|^2$ per lattice site, at the Γ point, of the wave functions corresponding to the two zero-energy end states of the 5-AGNR.

of topological edge states at the boundary of the AGNR with vacuum is dictated by the Z index and hence by the width and structure of the ribbon termination. In the case of metallic AGNRs, the number of TSSs is one unit less than the value of Z . Furthermore, for a specific type of termination, the number of localized end states increases with the ribbon width, one state for every six-atom increase of the width. Thus, in a chiral-symmetric system, the existence of zero-energy edge states is exactly correlated with the nonzero winding number and there are AGNRs, topologically trivial by the Z_2 classification, that exhibit TSSs at their borders.

IV. GRAPHENE NANORIBBON JUNCTIONS

Joining AGNRs of different widths allows one to engineer their electronic structure [46,47] and to realize that for electronic states localized at the interface, confined to an AGNR or extended to all the system, the differences arise from the topological character of the overall junction. If the junctions are organized in a periodic array, the electronic states may hybridize and form bands. Such bands have been designed and experimentally observed in one-dimensional arrays of AGNRs. The atomically precise synthesis of topological AGNR superlattices [17,18] has demonstrated that trivial and nontrivial electronic phases are created by the controlled periodic coupling between adjacent topological states at the junctions.

We have analyzed the electronic properties of AGNR junctions with diverse topological character, following the family classification. To this end, we have calculated the electronic structure of AGNR junctions of different widths with various structural couplings. Any junction of two AGNRs of different width, in which the number of atoms is preserved at the interface, can be formed by connecting the ribbons with one of the two geometries R1/R1 or R1/R2, i.e., either connecting two ribbons with the same R1 termination or with different endings R1 and R2, respectively. This is because these geometries are the only two different types of AGNR structural coupling without dangling bonds. When the two

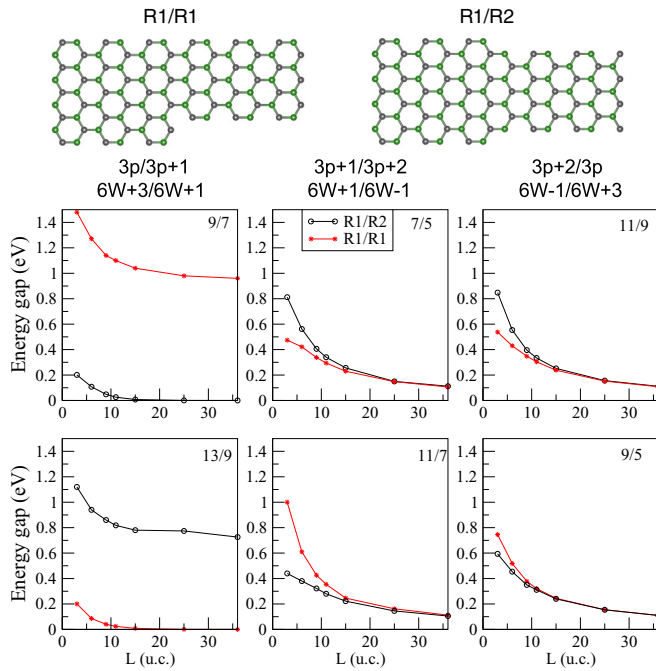


FIG. 6. Top: Schematics of the 9-7-AGNRs heterojunction unit cell structures with $\Delta N = 2$. Bottom: Dependence of the energy gap of the R1/R2 (open circles) and R1/R1 junctions with the length of the heterojunction expressed as the number of unit cells of the constituent ribbons for the three different types of superlattices. The difference between the width of the constituent ribbons is of two transverse rows (top) and of four transverse rows (bottom).

ribbons differ by only two rows of carbon atoms, the two types of structural coupling lead to two different structures: a symmetric junction with mirror and inversion symmetry and an asymmetric junction. If the difference in width is greater than two, more than one asymmetric geometry may occur. Figure 6 represents the structure of the unit cell of the 9-7 armchair graphene superlattice (AGSL) with the two types of coupling, the length of the constituent segments being 3 u.c.

We consider junctions of two AGNRs of different width arranged periodically as illustrated in Fig. 6, the width difference being $\Delta N = N_1 - N_2 = 2, 4, 6$, or 8, where N_1 and N_2 are the number of carbon rows of the constituent ribbons. When $\Delta N = 2, 4$, or 8, the two AGNRs belong to different families and three distinct cases are possible: $3p/3p + 1$, $3p + 1/3p + 2$, and $3p + 2/3p$. If $\Delta N = 6$, the two AGNRs belong to the same family. For each type of junction, we perform calculations for AGNRs of various widths with the two possible structures R1/R1 and R1/R2, in order to identify general trends, and we have studied different lengths of the constituent segments. By convention the wider AGNR always has the R1 termination. We discuss those structures with the narrowest AGNRs since the behavior is found to be equivalent for all the junctions of the same type.

Figure 6 presents the dependence of the energy gap between the highest occupied and lowest empty state with the length of the heterojunction for representative superlattices of the three distinct types of unions. Both connections R1/R1 and R1/R2 and $\Delta N = 2$ and 4 are displayed. The length is expressed as the number of unit cells of the constituent

ribbons; for these calculations, both segments are of the same length. The behavior is similar for junctions that include a metallic AGNR of the $3p + 2$ family, and differ in the type of coupling, R1/R1 or R1/R2. As the length of the AGNRs increases, the energy gap for the two different types of connection tends to zero. Conversely, the energy gap of the $3p/3p + 1$ junction, formed by two semiconductor AGNRs, shows a different dependence for both couplings. In each of the cases the differences between the energy gap behavior of junctions with $\Delta N = 2$ or 4 are minimal.

These results can be understood in terms of the junction topology, which is determined by the width and 1D bulk unit cell of the constituents AGNRs. Table II shows the relation between the topological invariants of the two AGNRs forming the three possible types of unions, with a width difference of two, four, and eight C rows. The invariants are given for the unit cell RJ , where J is equal to 1 or 2. For each type of junction, the relation between the topological invariants of all the superlattices (SLs) that differ by the same number of C rows is the same. For example, for junctions $3p/3p + 1$ and $\Delta N = 2$, such as 9-7, 15-13, or 21-19, the Z_2 and Z invariants are the same for the two ribbons, when they have the same unit cells. Therefore, the topological junction will be formed by two ribbons with different unit cells. On the contrary, when the ribbons differ by four C rows, i.e., 3-7 or 9-13, Z_2 and Z are different for the two AGNRs with the same unit cells and consequently the topological junction is formed by AGNRs with the same unit cells. Therefore, Table II provides a procedure for designing both nominal trivial and topological junctions and SLs. Next, we present results for the three types of AGSL and compare them with the predictions of Table II.

A. Two-semiconductor junctions

As Table II shows, for a specific unit cell the constituent AGNRs of any $3p/3p + 1$ junction with $\Delta N = 2$, i.e., 9-7, 15-13, 21-19, etc., belong to the same Z_2 and Z topological class. Therefore, without loss of generality, we focus on the superlattice (AGSL) formed by 9- and 7-AGNRs with the larger band gaps. Figure 7 shows the dispersion relations of the 9-7-AGSL for the two structural couplings, R1/R1 and R1/R2; calculations have been performed with segments of 6 u.c. length of each constituent ribbon. While the former presents a large band gap, two symmetric energy bands appear at low energy in the symmetric R1/R2 9-7-AGSL, whose constituent AGNRs belong to distinct topological classes (see Tables I and II). These topologically protected states exhibit a strong localization at the interface between the two AGNRs, whereas those defining the band gaps in both structurally different heterojunctions spread over only one AGNR. Increasing the length of the segments, the energy bands become denser and the gaps decrease toward ≈ 0.9 eV, the band gap of the 9-AGNR and the smallest gap of the junction constituents. Moreover, the energy of the topological bands goes to zero and the wave functions remain localized at the interface and mainly confined in a sublattice. In order to show the difference between the TSs and the confined states the wave function distributions per lattice site, obtained at the Γ point of the BZ, are schematically depicted in Fig. 7 for the first state of each of the two SL types, R1/R2 and R1/R1. It also shows

TABLE II. Relation between the topological invariants, Z_2 and Z , of the two ribbons forming the three different types of AGSLs, for the two R1 and R2 u.c. and for width differences $\Delta N = 2, 4$, and 8 C rows. The relation between the Z_2 invariants is written for the R1 geometry; the sign changes for the R2 u.c., and therefore the ± 1 have to be changed to ∓ 1 for the R2 geometry.

ΔN	$3p/3p' + 1$ $6W + 3/6W' + 1$		$3p + 1/3p' + 2$ $6W + 1/6W' - 1$		$3p + 2/3p'$ $6W - 1/6W' + 3$	
2	$p' = p - 1$ $W' = W$	$Z'_2(\text{RJ}) = Z_2(\text{RJ})$ $Z'(\text{RJ}) = Z(\text{RJ})$	$p' = p - 1$ $W' = W$	$Z'_2(\text{RJ}) = Z_2(\text{RJ})$ $Z'(\text{RJ}) = Z(\text{RJ})$	$p' = p$ $W' = W - 1$	$Z'_2(\text{RJ}) = Z_2(\text{RJ}) + 1$ $Z'(\text{RJ}) = Z(\text{RJ}) - 1$
4	$p' = p + 1$ $W' = W + 1$	$Z'_2(\text{RJ}) = Z_2(\text{RJ}) - 1$ $Z'(\text{RJ}) = Z(\text{RJ}) + 1$	$p' = p + 1$ $W' = W + 1$	$Z'_2(\text{RJ}) = Z_2(\text{RJ}) - 1$ $Z'(\text{RJ}) = Z(\text{RJ}) + 1$	$p' = p + 2$ $W' = W$	$Z'_2(\text{RJ}) = Z_2(\text{RJ})$ $Z'(\text{RJ}) = Z(\text{RJ})$
8	$p' = p - 3$ $W' = W - 1$	$Z'_2(\text{RJ}) = Z_2(\text{RJ}) + 1$ $Z'(\text{RJ}) = Z(\text{RJ}) - 1$	$p' = p - 3$ $W' = W - 1$	$Z'_2(\text{RJ}) = Z_2(\text{RJ}) + 1$ $Z'(\text{RJ}) = Z(\text{RJ}) - 1$	$p' = p - 2$ $W' = W - 2$	$Z'_2(\text{RJ}) = Z_2(\text{RJ})$ $Z'(\text{RJ}) = Z(\text{RJ}) - 2$

the spatial distribution of the wave function weights of the highest valence band states of both junctions, with 9- and 7-AGNR segments of 36 u.c. in length. Interestingly, for the 9-7-AGSL with large segments, the nontopological states of both junctions remain confined to the 9-AGNR segment and the second quantized state has a higher energy than the valence band of the 7-AGNR. Therefore, the electronic structure of the junctions is dictated by their topology.

When the width difference is $\Delta N = 4$, i.e., 3-7-AGSL, 13-9-AGSL, for a given unit cell type, either R1 or R2, the two constituent AGNRs belong to distinct topological classes (see Table II); hence, the topological junction corresponds to the R1/R1 geometry which turns out to be the symmetric one. As Fig. 6 shows, the energy gap dependencies on the SL length of the TSs and trivial states of the 13-9-AGSL are analogous to those of the 9-7-AGSL; even the localization of TSs at the interface is similar. Finally, for $\Delta N = 8$, i.e., 15-7-AGSL, the R1/R1 coupling also defines the topological phase and, as in the previous case, gives rise to the symmetric junction. However, due to the large number of unsaturated zigzag edges at the interfaces, the top of the valence band of the trivial SL, R1/R2, is also dominated by states mainly located at the free zigzag borders. This localization is enhanced when the length of the constituent ribbons is increased. Results for the 15-7-AGSL for two different couplings of the AGNRs are shown in Fig. 8 for two different lengths of the SL constituent segments, 6 and 36 u.c.

Consequently, all $3p/3p + 1$ semiconducting junctions feature topologically protected interface states for at least one AGNR connection type.

B. Metal-semiconductor junctions

Next, we investigate the special case of junctions that contain $N = 3p + 2$ AGNRs. Without considering the perturbation induced by the structural relaxation of the side edge atoms, the band gap of $3p + 2$ AGNRs closes at the Fermi level at Γ . However, Jiang *et al.* [22] generalized the Z index to metallic ribbons and obtained the same expressions as for the semiconductor AGNRs. When $\Delta N = 2$, the allowed junctions are $3p + 1/3p + 2$ (7-5, 13-11, etc.) and $3p + 2/3p$ (11-9, 17-15, etc.), keeping the rule that the wider ribbon with R1 u.c. is at the first place. Notice that in the case of $3p + 1/3p + 2$ AGSLs the topologically nontrivial junction would

be R1/R2 while in the case of the $3p + 2/3p$ AGSL it would be the R1/R1 junction, according to Table II.

The dispersion relations of the representative 7-5-AGSL ($3p + 1/3p + 2$) are displayed in Fig. 9 for the symmetric R1/R2 and asymmetric R1/R1 connections. Although there is a small difference between the values of the band gap of both junctions, the energy distribution of the bands around zero, as well as the spatial localization of the $|\phi|^2$, are analogous regardless of the topology of the AGNRs. In both cases, the states are found on the metallic ribbon, although the largest density of wave function amplitude is on the atoms of the interfaces, particularly in the asymmetric R1/R1 junction, which is a topologically trivial system according to the classification given in Ref. [22]. Note that even for AGNR segments as long as 36 u.c. there is a significant gap of ≈ 0.1 eV in both SLs.

The behavior of the ($3p + 2/3p$) 11-9-AGSL (not shown) is similar to that of the previous junction, the bands around zero energy being also located in the metallic AGNR irrespective of the topological character of the system. Likewise, junctions between ribbons whose widths differ by four rows of atoms, $\Delta N = 4$, as 11-7- or 9-5-AGSLs, show the same features as those that differ by two, $\Delta N = 2$. In the $\Delta N = 4$ SLs, the topological phase would appear for the R1/R1 connection for the $3p + 1/3p + 2$ AGSLs and for the R1/R2 connection for the $3p/3p + 2$ AGSLs although the states are found in the metallic ribbon and not restricted to a sublattice. These results are implicit in the evolution of the energy gaps with the SL length shown in Fig. 6; the gap difference between the two coupling geometries is drastically reduced from a length of about 15 u.c.

However, when $\Delta N = 8$, analogously to the semiconductor SLs, topologically nontrivial and trivial SLs present interface states. The band structure of the $3p + 1/3p + 2$ 13-5-AGSL for the R1/R1 symmetric junction presents an in-gap state very close to zero energy with $|\phi|^2$ localized mainly in the boundary atoms. For the trivial asymmetric R1/R2 junction the band gap is larger and, although a part of the highest occupied state $|\phi|^2$ localizes at the boundaries, there is some weight extended across the $3p + 2$ segment. Figure 10 shows the dispersion relation for the $3p + 2/3p$ 17-9-AGSL with the trivial symmetric R1/R1 and nontrivial asymmetric R1/R2 connections, according to the Ref. [22] classification. Localized interface states emerge in both cases, although as in semiconductor AGSLs, the TS extends along all the interface

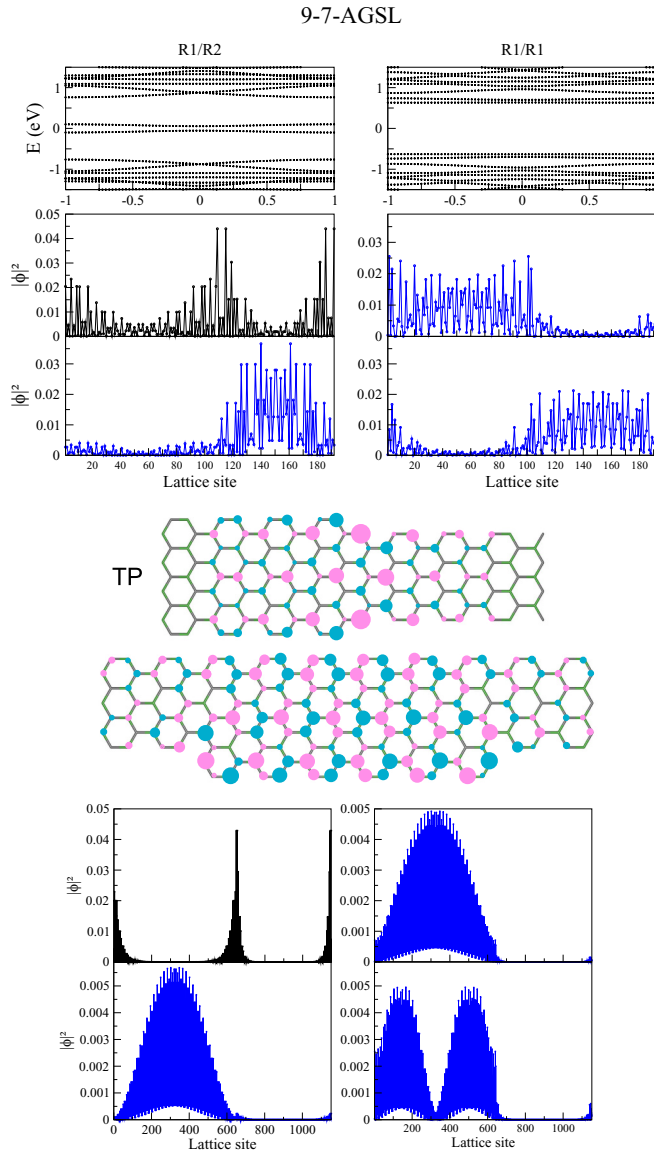


FIG. 7. Top: Band structure of the 9-7-AGSL formed by 6 u.c. length segments. Bottom: Wave function amplitude density $|\phi|^2$ per lattice site across the SL, at the Γ point, for the two first occupied states. Results calculated for the R1/R2 symmetric structure (left) and for the nonsymmetric R1/R1 (right). Wave function distributions per lattice site, corresponding to the first state of each SL type, are depicted in blue (pink) circles indicating positive (negative) amplitudes. For comparison, the $|\phi|^2$ per lattice site when the length of each of the constituent ribbons is 36 u.c. is shown below.

atoms, while the trivial states are centered on the free zigzag edges. The R1/R1 junction despite being trivial presents an in-gap state at energy close to zero as in the two previous 15-7- and 13-5-AGSLs.

C. Junctions formed by ribbons of the same family

We have also investigated AGSLs formed by ribbons of the same family. In this case $\Delta N = 6$ and 13-7-, 15-9-, and 11-5-AGSLs are representative of $3p + 1$, $3p$, and $3p + 2$ families, respectively. The SLs formed by ribbons belonging

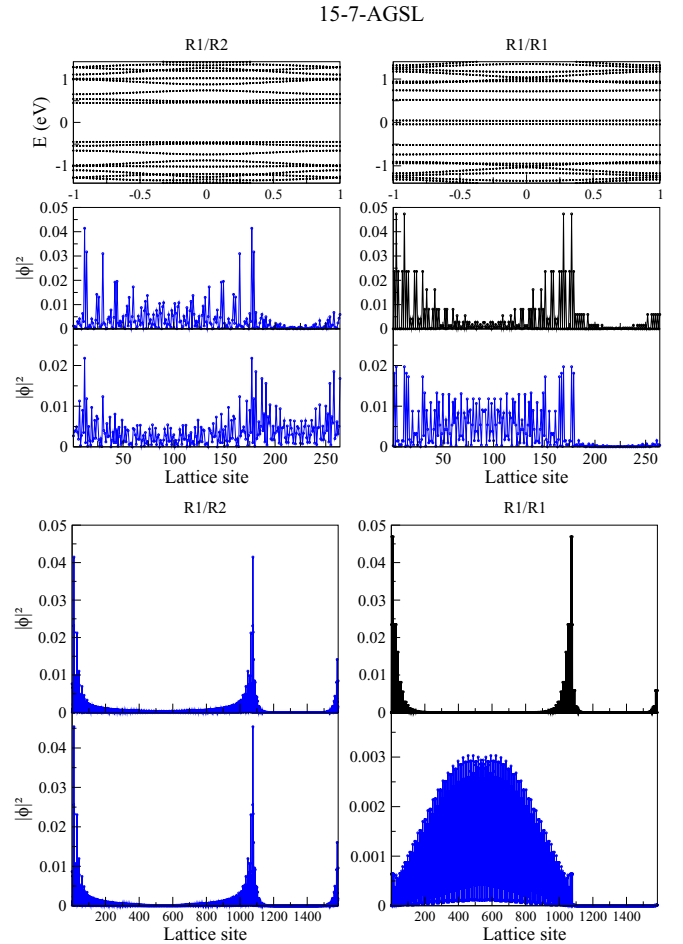


FIG. 8. Top: Band structure of the 15-7-AGSL formed by 6 u.c. length segments. Bottom: Wave function amplitude density $|\phi|^2$ per lattice site across the SL, at the Γ point, for the two first occupied states. Results calculated for the R1/R2 nonsymmetric junction (left) and for the R1/R1 symmetric junction (right). Below the $|\phi|^2$ distributions versus lattice sites are shown for SLs made by 36 u.c. length segments.

to the semiconductor families $3p$ and $3p + 1$ present a topological phase for the R1/R1 asymmetrical connection (see Table II and Fig. 11). However, for metallic $3p + 2$ junction, analogous to the previously discussed junctions containing a metallic AGNR, the nominally topological junctions do not show an interface localized state.

In all the AGSLs studied, the number of C-C links at the interface between the constituent ribbons is always one less in connection R1/R1 than in connection R1/R2. However, we have found topological states located at the interface with both kinds of connections depending on the family types of junction and on ΔN . Therefore, our results do not support the claim that the minimum number of C-C bonds in the interface is determinant for the development of states located at the interface [48].

D. Finite-length junctions: End and junction states

All the results discussed above have been obtained for AGSLs calculated with periodic boundary conditions. We

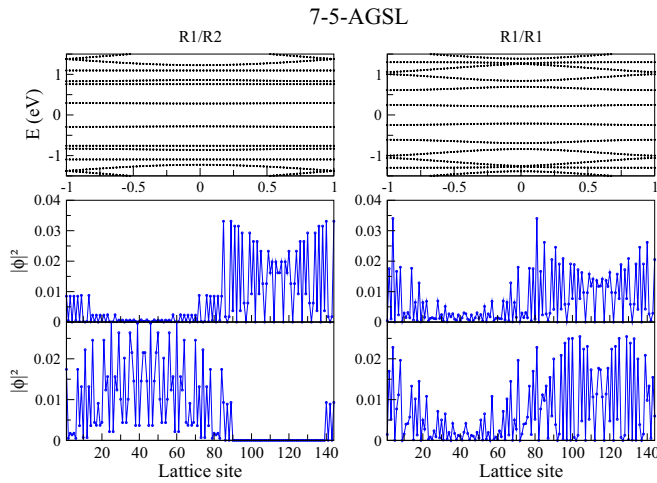


FIG. 9. Top: Band structure of the 7-5-AGSL formed by 6 u.c. length segments. Bottom: Wave function amplitude density $|\phi|^2$ per lattice site across the SL, at the Γ point, for the two first occupied states. Results calculated for the R1/R2 symmetric junction (left) and for the R1/R1 nonsymmetric junction (right).

have also investigated finite-size junctions of different types and sizes in order to gain insight into the interrelation between end and topological junction states. Experimental results from the finite-size 9-7-AGSL [17] have reported, besides the TSs, end states at the boundaries between the heterojunction termini and vacuum and the importance of correlation in these states have been investigated [49]. For junctions formed by semiconductor ribbons, there is a clear difference between the topological and trivial cases. Figure 12 presents the electronic properties of 13-7 AGNR junctions, both trivial and topological, of finite length, specifically 16 u.c. each segment. Those corresponding to the periodic AGSLs have been just discussed and represented in the previous figure. In both cases edge states confined at the termini of the constituent segments are present at zero energy. In addition, some meV

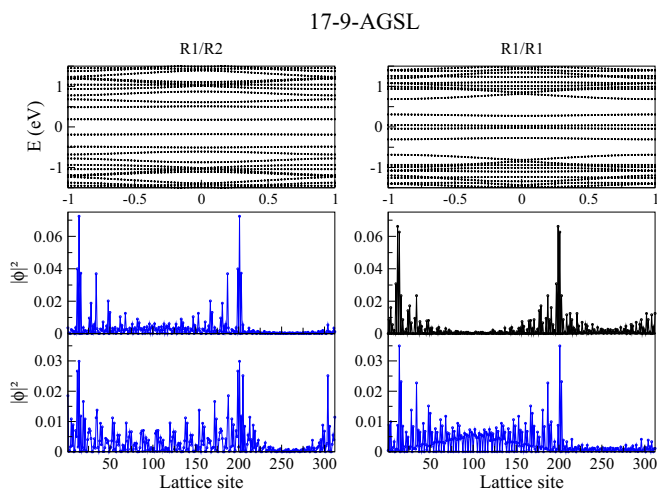


FIG. 10. Same as Fig. 9 for the 17-9-AGSL formed by 6 u.c. length segments. Results calculated for the R1/R2 nonsymmetric junction (left) and for the R1/R1 symmetric junction (right).

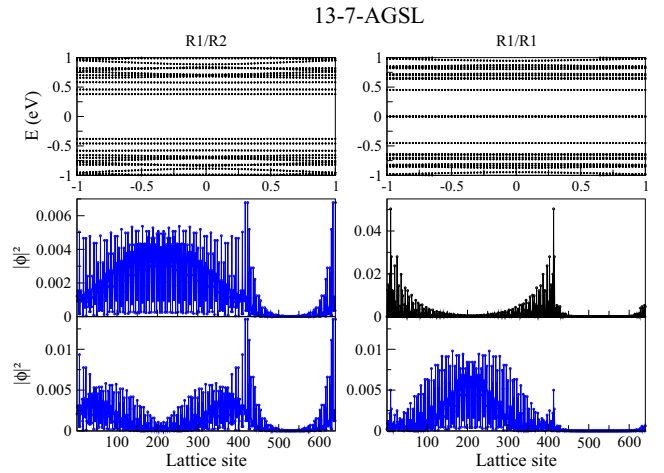


FIG. 11. Same as in Fig. 9 for the 13-7-AGSL formed by 16 u.c. length ribbons, both of the $3p + 1$ family. Results for the R1/R2 symmetric junction (left) and for the R1/R1 non-symmetric junction (right).

below, the topological state appears localized at the boundaries between the two ribbons and the 13-AGNR and vacuum in the topological junctions, while in the other geometry, the trivial case, a state with density probability localized in the two ends of the junction emerges, as can be observed in the top and middle panels of Fig. 12, where the $|\phi|^2$ distribution and the wave function amplitudes are represented, respectively. This difference between topologically trivial and nontrivial finite junctions was observed in Ref. [17] along with end states strongly dependent on the edge structure. In our results the zero-energy edge states also show dependence on the structure of the termini, as is clearly shown in the top panel of Fig. 12. The schematic distribution of the wave functions corresponding to the end and junction states of the nonsymmetric R1/R1 junction are depicted for a smaller heterojunction, segments of 6 u.c. length; therefore, the localization is less pronounced.

We only present here results for this heterojunction; finite AGNR junctions of 16 u.c. length of the $3p$ and $3p + 1$ families show similar behavior for $\Delta N = 2, 4$, and 6 . For finite-size junctions with one of the constituents from the metallic family, end states appear at both termini but for both coupling geometries the $|\phi|^2$ of the next state in energy is extended in the metallic segment. This behavior is common for SLs of $\Delta N = 2, 4$, and 6 ; however, for $\Delta N = 8$ we find the same difference as in the semiconductor SL as stated above.

V. DISCUSSION AND GENERAL REMARKS

As shown throughout the paper, the presence of edges and borders in graphene structures has strong implications for the low-energy spectrum of p electrons. In particular, GNRs show distinct electronic properties related to their edges. Due to the spatial and chiral symmetries of the graphene lattice, armchair-edge GNRs are one-dimensional topological materials and, depending on their width and the shape of the bulk unit cell, they belong to different topological classes. Hence, AGNRs are characterized by the invariants: Z_2 , determined by spatial and time-reversal symmetries, and/or Z , defined

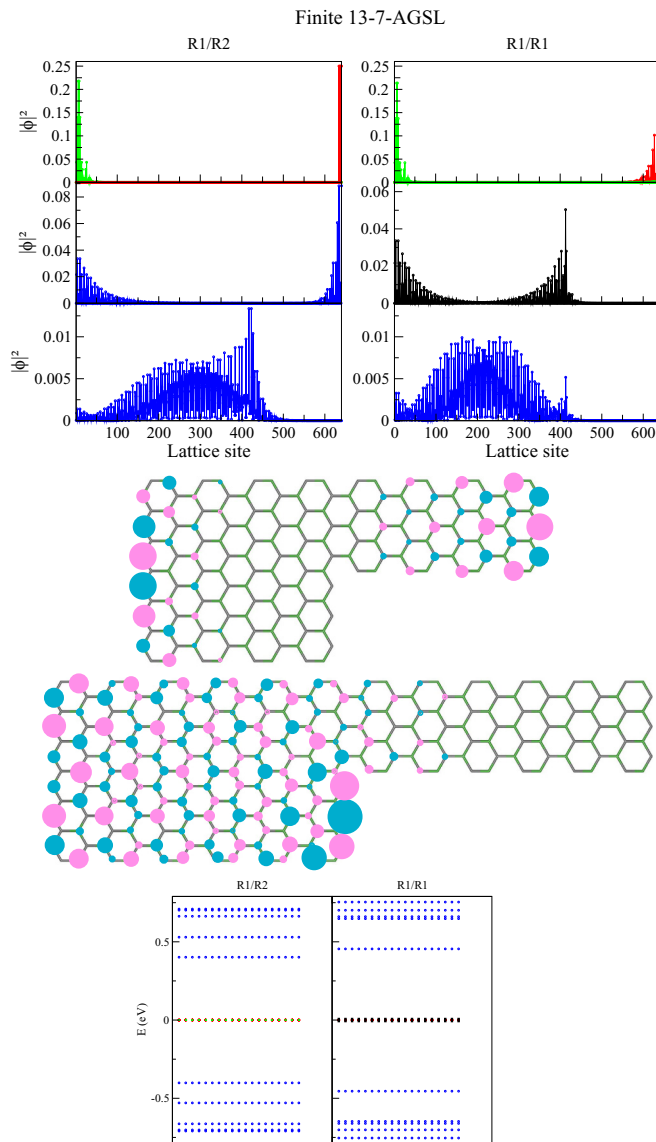


FIG. 12. Wave function amplitude $|\phi|^2$ per lattice site corresponding to zero-energy end states confined at the termini of the heterostructure (top), and the two next occupied states (middle and bottom) for the R1/R2 symmetric junction (left) and for the R1/R1 nonsymmetric junction (right), for a finite heterostructure formed by ribbons of 16 u.c. length. The wave function distributions per lattice site corresponding to the edge and junction states are schematically depicted for a 6 u.c. R1/R1 junction. Below, the energy spectrum of the finite 13-7-AGSL is shown for the two junction types.

by chiral symmetry. Periodic AGNRs only exhibit delocalized bands, whose wave functions extend along the ribbon, independently of their topological character. However, when frontiers and edges are present localized bound states exist at the borders.

On the basis of a tight-binding model, we have determined the topological invariants of AGNRs and elucidated the intriguing electronic properties of AGNRs with single or multiples interfaces. In a finite-length AGNR, besides the armchair edges along the length, there are two interfaces with vacuum that correspond to two short zigzag edges at

both ends. Whereas the armchair borders do not induce localized states, the zigzag terminations generate bound localized states. They originate from the boundary conditions, that is, from the requirement that the probability amplitude of the electrons must vanish beyond the carbon atoms at the edge. The emergence of conjugate zero-mode end states is closely related to the chiral symmetry of the AGNR and, therefore, to its topology. Actually, their existence is precisely correlated with a nonzero winding number. In semiconductor AGNRs, the number of edge states at each end, without counting the spin degree of freedom, is equal to the Z invariant, while in metallic AGNRs, in the absence of relaxation at the armchair borders or electronic correlations, the number is equal to one unit less than Z . Accordingly, we can readily work out the number of topological end states in the band gap, located at the boundaries of the AGNR, by controlling the width of the ribbon and the shape of the termination. We find that, for a given type of termination, the number of localized zero-mode end states generally increases with the ribbon width, and the energy separation between two conjugate topological end states, belonging to the valence and conduction bands, respectively, is defined by the length of the AGNR. Furthermore, the left and right edge states have opposite chirality and thus they have wave amplitudes exclusively at the A and B sublattices, respectively. These properties of the zero-mode end states allow the design of topological states simply by precisely controlling the structural parameters of the AGNR.

Similarly, the topological character of a junction is defined by the widths of the ribbons and their structural coupling at the interface. Therefore, topological bands emerge in AGSLs with a periodic modulation of their width whenever the interface coupling defines a junction of AGNRs with distinct topological character, either different Z_2 or Z . For junctions of semiconductor AGNRs of varied widths there is at least one type of connection that results in a topological junction. This junction supports topological states, whose wave function accumulates at the interface and is restricted to atoms of a single sublattice. When the junctions are arranged periodically the energy of these topological bands is dictated by the length of the constituent AGNR segments and they are robust against perturbations since they are well separated from the bulk states by the semiconducting energy gap of AGNRs. The presence of midgap states is quite robust against local perturbations. The stability of the junction states, protected by spatial symmetries, against local strain and vacancies has been confirmed by first-principles and tight-binding calculations [14,48]. On the other hand, end and junction states have been experimentally observed by scanning tunneling microscopy in different atomically precise AGSLs [17,18]. If the difference in the constituent ribbon widths is large, $\Delta N \geq 8$, states located on the zigzag atoms of the interface appear for any type of connection, the coupling barrier being the dominant effect. However, if both AGNRs belong to the same topological class, the junction is topologically trivial and the interface states are not chiral. They have wave function amplitude in both A and B sublattices and their energy is close to that of bulk states.

In the special case of AGSLs containing a metallic ribbon, junctions with different structural coupling show a similar electronic spectrum. The energy distribution of the bands around zero, as well as their spatial localization, are analogous

regardless of the topology of the AGNRs. For all AGSLs, the states are found on the metallic ribbon, although with a large amplitude at the interface atoms. Only when the width difference is ≥ 8 do topological and trivial bands accumulated at the interfaces develop. As in semiconductor junctions the topological bands are chiral, while the interface trivial states are not chiral.

Furthermore, in all the analyzed AGSLs, irrespective of the topology of the constituent ribbons, bulk states bracketing the topological interface states extend to only one AGNR. The highest valence and lowest conduction bands are located in the widest AGNR with the smallest energy gap. However, states located in each of the AGNRs alternate, since the energy and spatial distribution of the wave function of these bulk states follow the quantization pattern of confined states, analogously to the allowed states of a particle in a square potential well. The energy of the quantum-well-like bulk states depends on the length of the corresponding segment. This is a particularly unusual and exotic result, since effective electron confinement is produced in a graphene system.

Finite-length AGSLs, in addition to the in-gap topological modes, show edge states confined at the termini of both AGNRs. They are similar to those of the constituent finite AGNRs and, although they have close energy, the AGSL end states do not interact with the in-gap topological states accumulated at the interface atoms. Calculations with the four-orbital basis (see the Appendix), although without electron-hole symmetry, give the same results. The σ bands appear at energies below the highest valence band and the edge states of the isolated ribbons and of the heterojunctions are of π character like the interface states.

It is worth it to highlight the importance of the bipartite nature of the graphene lattice since the number of zero-energy states is related to the imbalance between the number of A and B sites or chiral charge [13,25]. The sublattice symmetry is on the basis of the design of topological phases in AGNRs and allows different strategies to investigate unknown phenomena and build new devices [7,10,11,30].

In summary, finite-length AGNRs and AGSLs provide a route to generate carrier confinement in nanoscale graphene. By controlling the structural parameters of AGNRs and AGSLs, topological bound states either at the extreme or at the interface between two distinct AGNRs can be tailored. In addition, states constrained to a single AGNR in AGNR heterojunctions and superlattices can also be induced. These confined states can be a source of peculiar magnetic and transport properties, since the Coulomb interaction in the topological bound states is expected to be much greater than the bandwidth [50,51], which suggests that they are unique systems to explore the effect of Coulomb interactions in one dimension.

ACKNOWLEDGMENTS

The authors thank J. I. Beltrán for fruitful conversations. M.P.L.-S. acknowledges financial support of Spanish MINECO under Grant No. PGC2018-099199-B-I00 and the European Union structural funds and the Comunidad Autónoma de Madrid (CAM) NMAT2D-CM Program

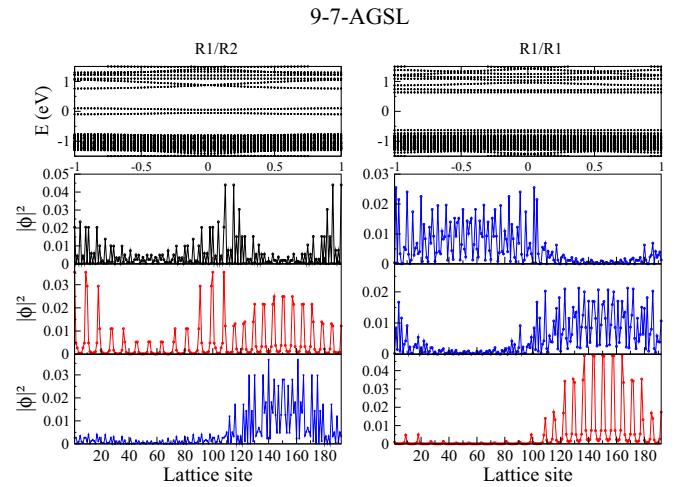


FIG. 13. Top: Band structure, calculated with the four-orbital basis, of the 9-7-AGSL formed by 6 u.c. length segments. Bottom: Wave function amplitude density $|\phi|^2$ per lattice site across the SL, at the Γ point, for the three first occupied states. Results calculated for the R1/R2 symmetric structure (left) and for the nonsymmetric R1/R1 (right). The σ wave function amplitude distributions per lattice site are represented in red.

(S2018-NMT-4511). M.C.M. acknowledges financial support of Spanish MINECO under Grant No. RTI2018-097895-B-C41 and the FEDER Program of the European Union.

APPENDIX

As stated in Sec. II, all the results presented in this work have been obtained by the TB approach with the four-orbital basis set and with the single π -orbital basis set. In order to show the coincidences and differences between the results obtained by both Hamiltonians, Fig. 13 depicts the four-orbital band structures and the module squared weight distribution per lattice site of the three first occupied states at the Γ point, corresponding to the R9-R7 SL for the R1/R2 symmetric

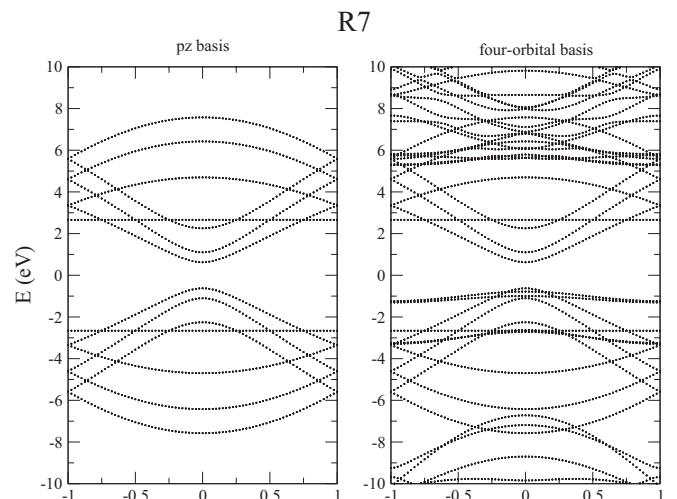


FIG. 14. Band structure of the R7, calculated with the p_z (left) and four-orbital (right) basis set Hamiltonians.

and R1/R1 asymmetric structures. The segment lengths are of 6 u.c. for both constituent ribbons. These results are directly comparable to those represented in Fig. 7 corresponding to the same SL obtained with the single p_z -orbital basis. In the R1/R2 SL, the in-gap states arise at the same energies and present the same character in both calculations. The wave function distributions per C atom are the same. The second occupied state, of σ character, is absent in Fig. 7, but the third occupied state, of π character, appears at the same energy and presents the same distribution per lattice site as the second one in Fig. 7. In the R1/R1 coupling the first and second bands are of π character and coincide with those of Fig. 7 in energy and distribution. The third occupied state is of σ character. The energy-gap values are the same in both calculations. Considering finite-size SLs, the edge states behave the same as those presented in Fig. 12. In the experimentally bottom-up synthesized AGNRs and SLs the σ orbitals of the carbon atoms at the borders are capped by hy-

drogen and therefore are not involved in the edge or junction states [13].

Therefore, in the energy region of interest both Hamiltonians give similar results. The band structure obtained with the four-orbital basis set lacks electron-hole symmetry, as can be observed in Fig. 14 where the band structures of R7 are depicted in the same energy interval. The p_z bands appear at the same energies, presenting the same symmetry and dispersion law. Although some σ bands lie at energies close to the valence band and do not intervene in the junction states. When considering finite-size ribbons, the end states are the same as those obtained with the p_z Hamiltonian for both the R1 and R2 geometries. The inclusion of the $2s$, $2p_x$, and $2p_y$ orbitals in the Hamiltonian is of interest in calculations of the intrinsic spin-orbit interaction (SOI) effects, in carbon nanotube calculations or curvature effects in graphene since both SOI and curvature induce hybridization of σ - π orbitals [33,52,53].

-
- [1] J. Cai, P. Ruffieux, R. Jaafar, M. Bieri, T. Braun, S. Blankenburg, M. Muoth, A. P. Seitsonen, M. Saleh, X. Feng, K. Müllen, and R. Fasel, *Nature* **466**, 470 (2010).
- [2] A. Kimouche, M. Ervasti, R. Drost, S. Halonen, A. Harju, P. M. Joensuu, J. Sainio, and P. Liljeroth, *Nat. Commun.* **6**, 10177 (2015).
- [3] L. Talirz, P. Ruffieux, and R. Fasel, *Adv. Mater.* **28**, 6222 (2016).
- [4] L. Talirz, H. Söde, T. Dumschlaff, S. Wang, J. Sanchez-Valencia, J. Liu, P. Shinde, C. Pignedoli, L. Liang, V. Meunier *et al.*, *ACS Nano* **11**, 1380 (2017).
- [5] J. Cai, C. A. Pignedoli, L. Talirz, P. Ruffieux, H. Söde, L. Liang, V. Meunier, R. Berger, R. Li, X. Feng, K. Müllen *et al.*, *Nat. Nanotechnol.* **9**, 896 (2014).
- [6] Y.-C. Chen, T. A. Cao, C. Chen, Z. Pedramrazi, D. Haberer, D. de Oteyza, F. Fischer, S. Louie, and F. Crommie, *Nat. Nanotechnol.* **10**, 156 (2015).
- [7] L. Yan and P. Liljeroth, *Adv. Phys. X* **4**, 1651672 (2019).
- [8] S. Zhao, G. B. Barin, T. Cao, J. Overbeck, R. Darawish, T. Lyu, S. Draocho, S. Wang, T. Dumschlaff, A. Narita *et al.*, *Nano Lett.* **20**, 1124 (2020).
- [9] K.-S. Lin and M.-Y. Chou, *Nano Lett.* **18**, 7254 (2018).
- [10] D. Rizzo, J. Veber, G. Jiang, R. McCurdy, T. Cao, C. Bronner, T. Chen, S. G. Louie, F. R. Fischer, and M. Crommie, *Science* **369**, 1597 (2020).
- [11] D. J. Trainer, S. Srinivasan, B. L. Fisher, Y. Zhang, C. R. Pfeiffer, S.-W. Hla, P. Darancet, and N. P. Guisinger, [arXiv:2104.11334](https://arxiv.org/abs/2104.11334).
- [12] J. Li, S. Sanz, N. Merino-Díez, M. Vilas-Varela, A. Garcia-Lekue, M. Corso, D. G. de Oteyza, T. Frederiksen, D. Peña, and J. I. Pascual, *Nat. Commun.* **12**, 5538 (2021).
- [13] F. Zhao, T. Cao, and S. G. Louie, *Phys. Rev. Lett.* **127**, 166401 (2021).
- [14] T. Cao, F. Zhao, and S. G. Louie, *Phys. Rev. Lett.* **119**, 076401 (2017).
- [15] J. Zak, *Phys. Rev. Lett.* **62**, 2747 (1989).
- [16] C. L. Kane and E. J. Mele, *Phys. Rev. Lett.* **95**, 226801 (2005).
- [17] D. Rizzo, G. Veber, T. Cao, C. Bronner, T. Chen, F. Zhao, H. Rodriguez, S. G. Louie, M. Crommie, and F. R. Fischer, *Nature (London)* **560**, 204 (2018).
- [18] O. Gröning, S. Wang, X. Yao, C. A. Pignedoli, G. Barin, C. Daniels, A. Cupo, V. Meunier, X. Feng, A. Narita *et al.*, *Nature (London)* **560**, 209 (2018).
- [19] J. Lawrence, P. Brandimarte, A. Berdonces-Layunta, M. Mohamed, A. Grewal, C. Leon, D. Sanchez-Portal, and D. G. de Oteiza, *ACS Nano* **14**, 4499 (2020).
- [20] A. D. Zdetsis and E. N. Economou, *Carbon* **1176**, 548 (2021).
- [21] Y.-L. Lee, F. Zhao, T. Cao, J. Ihm, and S. Louie, *Nano Lett.* **18**, 7247 (2018).
- [22] J. Jiang and S. G. Louie, *Nano Lett.* **21**, 197 (2021).
- [23] G. Tamaki, T. Kawakami, and M. Koshino, *Phys. Rev. B* **101**, 205311 (2020).
- [24] Y. Jeong and S.-R. E. Yang, *Ann. Phys.* **385**, 688 (2017).
- [25] M. Guzmán, D. Bartolo, and D. Carpentier, [arXiv:2002.02850](https://arxiv.org/abs/2002.02850).
- [26] D. Tománek and S. G. Louie, *Phys. Rev. B* **37**, 8327 (1988).
- [27] R. Saito, G. Dresselhaus, and M. S. Dresselhaus, *Physical Properties of Carbon Nanotubes* (Imperial College Press, London, 1998).
- [28] A. H. Castro Neto, F. Guinea, N. M. R. Peres, K. S. Novoselov, and A. K. Geim, *Rev. Mod. Phys.* **81**, 109 (2009).
- [29] E. Kogan, V. U. Nazarov, V. M. Silkin, and M. Kaveh, *Phys. Rev. B* **89**, 165430 (2014).
- [30] S. Wang, N. Kharche, E. Costa-Girão, X. Feng, K. Müllen, V. Meunier, R. Fasel, and P. Ruffieux, *Nano Lett.* **17**, 4277 (2017).
- [31] M. Ezawa, *Phys. Rev. B* **73**, 045432 (2006).
- [32] L. Brey and H. A. Fertig, *Phys. Rev. B* **73**, 235411 (2006).
- [33] M. P. López-Sancho and M. C. Muñoz, *Phys. Rev. B* **83**, 075406 (2011).
- [34] Y.-W. Son, M. L. Cohen, and S. G. Louie, *Phys. Rev. Lett.* **97**, 216803 (2006).
- [35] P. H. Jacobse, A. Kimouche, T. Gebraad, M. M. Ervasti, J. M. Thijssen, P. Liljeroth, and I. Swart, *Nat. Commun.* **8**, 119 (2017).
- [36] J. Yamaguchi *et al.*, *Commun. Mater.* **1**, 36 (2020).

- [37] L. Yang, C.-H. Park, Y.-W. Son, M. L. Cohen, and S. G. Louie, *Phys. Rev. Lett.* **99**, 186801 (2007).
- [38] H. Zheng, Z. F. Wang, T. Luo, Q. W. Shi, and J. Chen, *Phys. Rev. B* **75**, 165414 (2007).
- [39] K. Wakabayashi, K.-i. Sasaki, T. Nakanishi, and T. Enoki, *Sci. Technol. Adv. Mater.* **11**, 054504 (2010).
- [40] S. Ryu and Y. Hatsugai, *Phys. Rev. Lett.* **89**, 077002 (2002).
- [41] R. D. King-Smith and D. Vanderbilt, *Phys. Rev. B* **47**, 1651 (1993).
- [42] D. Vanderbilt, *Berry Phases in Electric Structure Theory* (Cambridge University Press, Cambridge, UK, 1993).
- [43] P. Delplace, D. Ullmo, and G. Montambaux, *Phys. Rev. B* **84**, 195452 (2011).
- [44] J.-W. Rhim, J. Behrends, and J. H. Bardarson, *Phys. Rev. B* **95**, 035421 (2017).
- [45] Y.-D. Wu, [arXiv:1706.02370](https://arxiv.org/abs/1706.02370).
- [46] H. Sevinçli, M. Topsakal, and S. Ciraci, *Phys. Rev. B* **78**, 245402 (2008).
- [47] D. Prezzi, D. Varsano, A. Ruini, and E. Molinari, *Phys. Rev. B* **84**, 041401(R) (2011).
- [48] Y. Lv, Q. Huang, S. Chang, H. Wang, J. He, C. Wei, A. Liu, S. Ye, and W. Wang, *Phys. Rev. Appl.* **11**, 024026 (2019).
- [49] J.-P. Joost, A.-P. Jauho, and B. Michael, *Nano Lett.* **19**, 9045 (2019).
- [50] M. P. López-Sancho, F. de Juan, and M. A. H. Vozmediano, *Phys. Rev. B* **79**, 075413 (2009).
- [51] M. P. López-Sancho and L. Brey, *2D Mater.* **5**, 015026 (2018).
- [52] L. Chico, M. P. López-Sancho, and M. C. Muñoz, *Phys. Rev. B* **79**, 235423 (2009).
- [53] H. Santos, M. C. Muñoz, M. P. López-Sancho, and L. Chico, *Phys. Rev. B* **87**, 235402 (2013).